Biosensors and Bioelectronics 131 (2019) 30–36

Contents lists available at ScienceDirect

Biosensors and Bioelectronics

journal homepage: www.elsevier.com/locate/bios

Fabrication of N-doped multidimensional carbon nanofibers for high-performance cortisol biosensors

Goeen Jeong, Jungkyun Oh, Jyongsik Jang*

School of Chemical and Biological Engineering, College of Engineering, Seoul National University, 1 Gwanakro, Gwanakgu, Seoul 08826, Republic of Korea

ARTICLE INFO

Keywords:
Vapor deposition polymerization
N-doped carbon nanofiber
FET type biosensor
Cortisol

ABSTRACT

Cortisol is an hormone that regulates blood pressure, glucose levels and carbohydrate metabolism in humans. Abnormal secretion of cortisol can cause various symptoms closely linked to psychological and physical health. In this study, high-performance field-effect transistor (FET)-based biosensors for cortisol detection were fabricated from N-doped multidimensional carbon nanofibers. Nanofiber morphology was controlled by tailoring the pressure conditions during vapor deposition polymerization (VDP). Thereafter, conductive channels of FET were completed by thermal annealing, acid treatment, and antibody attachment. Changes associated with chemical processes were characterized by various instruments. The resulting transducers exhibited a rapid response toward cortisol molecules with accurate selectivity, stable reusability, and high sensitivity. Minimum detection level were as low as 100 aM with a wide linear detection range of 100 aM to 10 nM due to the large surface area of the transducer and a correspondingly high number of antibody labels. The response and applicability of these cortisol biosensors were also assessed using saliva as a test matrix.

1. Introduction

Cortisol detection is a crucial issue because its abnormal level heavily influences the quality of life. Cortisol, a stress biomarker, is important for the regulation of blood pressure, glucose levels and carbohydrate metabolism in response to environmental factors and the circadian rhythm (Kaushik et al., 2013; Corbalán-Tutau et al., 2014). Even abnormal secretion of cortisol can result in several harmful symptoms and diseases, such as Cushing's syndrome, Addison's disease, weakening of the immune system, increased levels of amino acids in the blood, obesity, heart attack, depression, and post-traumatic stress disorder (PTSD) (Arya et al., 2010a, 2010b; Kaushik et al., 2013). Thus, the importance of cortisol level management has been highlighted because the symptoms of unregulated cortisol excretion are closely linked with human life and health. Various techniques have been proposed already for continuous monitoring of cortisol level, such as enzyme-linked immunosorbent assays (ELISAs), radioimmunoassays (RIAs) and flow immunoassays. Nevertheless, these methods have definite disadvantages like time-consuming, and requires a relatively large volume of sample and complicated experimental reactions that must be performed by highly trained laboratory staff (Cook et al., 1997; Sarkar et al., 2007; Manickam et al., 2017).

Nowadays, increasing need for a fast, real-time and reliable medical diagnosis has led to growing interest in continuous monitoring of cortisol secretion. Thus, electrochemical biosensors including electrochemical impedance spectroscopy (EIS), high performance liquid chromatography (HPLC), fluorometric assays, and reverse-phase chromatography, have been developed for their low cost, mass fabrication, fast response and high sensitivity. (Arya et al., 2010a, 2010b; Tlili et al., 2011; Gangopadhyay et al., 2012; Kaushik et al., 2013; Kim et al., 2015, 2017; Sun et al., 2017)

Among the electrochemical cortisol biosensors available today, field-effect transistor (FET)-based biosensors especially boast relatively simple implementation into portable devices, miniature systems, and point-of-care (POC) applications. FET-based biosensors monitor changes in current through an FET transducer in response to an analyte binding to specific recognition systems, including enzymes, antibodies, nucleic acids and microorganisms, under a constant electric field (Moraes and Kubota, 2016). Such systems boast ultra-high sensitivity, excellent selectivity, real-time response, reusability, and cost-effective fabrication. Moreover, in liquid-ion gated FET-based biosensors, the gate dielectric layer is replaced with an electrolyte solution. This results in extremely rapid responses and improved signal transduction under low-voltage electric fields (Son et al., 2016a, 2016b; Ahn et al., 2016; An and Jang, 2017; Jang et al., 2018).

The various allotropes of carbon nanomaterials, such as graphene,

* Corresponding author.
E-mail address: jsjang@plaza.snu.ac.kr (J. Jang).

https://doi.org/10.1016/j.bios.2019.01.061
Received 8 November 2018; Received in revised form 9 January 2019; Accepted 22 January 2019
Available online 05 February 2019
0956-5663/

fullerenes, and nanofibers, have been used in many biosensing applications due to their extraordinary electrical, optical and mechanical properties (Punetha et al., 2017; Gokoglan et al., 2017; Thapa et al., 2017; Gupta et al., 2018). Nanofibers particularly exhibit high charge carrier mobilities along their axis of rotation, easy processability, and chemical stability (Kwon et al., 2012a; Geier et al., 2016). However, the semiconducting properties of pure carbon nanofibers are insufficient for high-performance, FET-based biosensors (Kwon et al., 2012a). Nevertheless, the semiconducting properties of carbon nanofibers could be improved via chemical doping, which can be applied to tune the band gap of the carbon lattice (Kwon et al., 2012a). In particular, doping with nitrogen atoms can have a tremendous effect on the electronic behavior of carbon nanofibers (Di Valentin et al., 2007). In addition, nitrogen species act as electron donors and can produce n-type transistor behavior in carbon fiber transducers (Wang et al., 2009; Brownlie and Shapter, 2018).

To enhance performance, the surface area of carbon nanofibers can be enhanced by introducing multidimensional structures via vapor deposition polymerization (VDP) (Jang et al., 2005; Kwon et al., 2012b). In VDP, vaporized monomer diffuses and polymerizes uniformly onto a suitable template without any stabilizers or surfactants (Zhao et al., 2000, 2015; Cho et al., 2010). The morphology and thickness of the polymer layer can be controlled by simply adjusting the deposition parameters, including the type of initiator, reaction time, temperature and pressure (Jyongsik and Byungkwon, 2003; Lee et al., 2015). In particular, the pressure in the VDP chamber affects the kinetics of polymerization and, ultimately, the morphology of the polymer film (Kwon et al., 2012c). Therefore, controlling the deposition parameters allows multidimensional control of the morphology of the conductive polymer layer, and enables polymer structures to be tailored for maximal sensitivity in FET-based biosensors (Li et al., 2007; Bai et al., 2011).

In this study, N-doped multidimensional carbon nanofibers were fabricated via electrospinning, VDP, and carbonization. They were then employed in the transducer layers of FET-based cortisol biosensors. The morphology of transducer layer was controlled by adjusting the pressure in the VDP chamber during deposition. Transducer layers deposited under vacuum were smooth, while those deposited at atmospheric pressure contained needle-like features. The real-time minimum detectable concentration of antibody attached to fibers that had been deposited at atmospheric pressure (AA_PCANFs) was 10^4 times lower than that of antibodies deposited under vacuum (VA_PCANFs). Thus, the larger surface area of AA_PCANFs effectively enhanced the performance of the transducer. FETs made with AA_PCANFs were also evaluated in real-time with salivary cortisol.

2. Materials and methods

2.1. Materials

Poly(vinyl alcohol) (PVA, MW 85,000), ferric (III) chloride ($FeCl_3$, 97%), methanol (≥99.9%), pyrrole (98%), (3-aminopropyl) triethoxysilane (APS, 98%), 4-(4,6-dimethethoxy-1,3,5-triazin-2-yl)-4-methylmorpholimium chloride (DMT-MM), hydrocortisone (≥ 98%), cortisol antibody (F4P1A3), neuron-specific enolase from human brain (NSE, ≥ 95%), prostate specific antigen from human semen (PSA, ≥ 99%) and epidermal growth factor from mouse (EGF) were purchased from Sigma-Aldrich.

2.2. Fabrication of N-doped carbon nanofiber transducers

A PVA solution was prepared by dissolving 0.8 g of PVA in 10 mL of distillated water with vigorous stirring at room temperature. The polymer solution was electrospun with an applied voltage of 16 kV and a flow rate of 5.5 μL min^{-1} and a 15-cm fixed collector distance. The electrospun PVA nanofibers were dipped in 9 wt% ferric chloride solution in methanol. Then, polypyrrole (PPy) was polymerized onto PVA nanofibers at 100 °C, using previously determined conditions of time and pressure, via vapor deposition polymerization (VDP). The resulting PPy nanofibers (PPyNFs) were then subjected to two successive thermal treatments: stabilization at 135 °C for 2 h in air and carbonization at 600 °C for 1 h under an argon atmosphere. Afterwards, the carbonized PPyNFs (PCNFs) were immersed in a 3:1 (v/v) mixture of 1 M sulfuric acid and 1 M nitric acid for 6 h and washed with distillated water. The acid-treated PCNFs (PCANFs) were then soaked in a dilute solution of anti-cortisol antibody in a solution of phosphate-buffered saline (PBS, pH 7.4) and 1 wt% aqueous DMT-MM for 12 h, washed with distilled water, and dried at room temperature.

2.3. Fabrication of FET-based biosensors

Interdigitated array (IDA) electrodes were treated with 5 wt% aqueous APS for 6 h to amino-functionalize the surface of the glass substrate. The 1 wt% solution of antibody-labeled carbon nanofibers in acetone was prepared and dropped onto the electrodes. After drying, the electrodes were exposed to 1 wt% aqueous DMT-MM and dried at room temperature.

2.4. Electrical measurements with FET-based biosensors

FET-based biosensors were built with a liquid-ion gate of PBS solution (pH 7.4). Current was measured at room temperature using a Keithley 2612A source meter (Keithley Instruments, Inc., Cleveland, OH, USA) and normalized as follows;

$$\left[\frac{\Delta I}{I_o}\right]_{SD}(\%)=\frac{(I-I_o)}{I_o}\times 100$$

where I_o indicates the initial current and I is the real-time measured current.

2.5. Instrumentation

Scanning electron microscopy (SEM) was performed with a JSM-6701F (JEOL, Tokyo. Japan) microscope. X-ray photoelectron spectra (XPS) were obtained using a Sigma Probe (Thermo-VG, East Grinstead, UK). Raman and Fourier transform infrared (FT-IR) spectra were acquired with T64000 (Horiba Jobin Yvon, France) and Frontier (PerkinElmer, Waltham, MA, USA) spectrometers, respectively. All electrical measurements were performed with a Keithley 2612A source meter (Keithley Instruments, Inc.) and a probe station (model 4000; MS Tech, Hwaseong, South Korea).

3. Results and discussion

3.1. Fabrication of needle-like N-doped carbon nanofibers

Fig. S1 illustrates the fabrication of polypyrrole nanofibers (PPyNFs) via electrospinning and VDP. Poly(vinyl alcohol) (PVA) nanofibers were fabricated by electrospinning and used as the template for polymer growth. Electrospun nanofibers are effectively one-dimensional (1D) nanomaterials and facilitate charge mobility along their long axes by permitting efficient electron transport and enhanced charge carrier density (Shin et al., 2014; Kwon et al., 2010). The production of thin and uniform PVA nanofibers requires suitable electrospinning conditions that take into account multiple factors, including the concentration of the precursor solution, the applied electrical potential, and the distance to the collection plate (Supaphol and Chuangchote, 2008). Optimal films of PVA were obtained with an 8 wt % aqueous solution and a flow rate of 5.5 μL min^{-1}, with an applied potential of 16.0 kV. Electrospun nanofibers made under these conditions were ca. 120 nm in diameter (Fig. 1a).

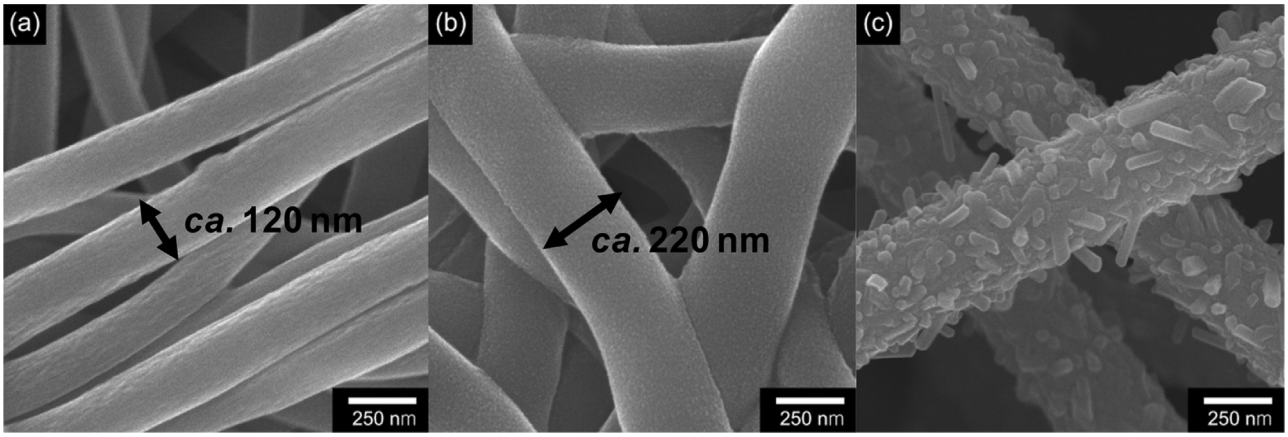

Fig. 1. Scanning Electron Microscopy (SEM) images of (a) PVA nanofibers, (b) PPyNFs from vacuum VDP method, (c) PPyNFs from atmospheric VDP method.

A methanolic solution of ferric (III) chloride ($FeCl_3$) was used as an initiator for the deposition of conducting polymer onto the surface of electrospun PVA nanofibers. The PVA nanofibers were dipped into the initiator solution. Charge-charge interactions between Fe^{3+} ions in the initiator solution and the partial negative charges of oxygen atoms in PVA resulted in the adsorption of trivalent iron onto the PVA surface. Adsorbed Fe^{3+} ions were then exposed to pyrrole monomer during VDP, resulting in oxidative polymerization on the PVA surface (Powell et al., 2017; Shin et al., 2014). Methanol was used as the solvent in the initiator solution because the formation of hydrogen bonds between methanol and pyrrole during polymerization can increase the conductivity of the resulting polypyrrole (PPy) (Machida et al., 1989). Moreover, the dipole moment of pyrrole increases due to charge transport along the polymer chain and chain orientation during polymerization (Lee et al., 2015).

Pressure and temperature play key roles in determining film morphology during VDP (Lee et al., 2015). Various PPy features were observed as a function of pressure in the VDP chamber. Needle-like PPy features were observed following VDP at atmospheric pressure. In contrast, the PVA film was evenly coated to a thickness of ca. 50 nm when PPy was deposited under vacuum. These morphological differences are evident in the scanning electron micrographs shown in Fig. 1b and c. The PPy layer grew via a nucleation-growth mechanism, its morphology being determined by the kinetic and thermodynamic conditions of the VDP step (Zhao et al., 2000). The ion-infused PVA substrate enhanced the π-π conjugation length of PPy by supplying dopant ions to the heteroaromatic backbone (Kim et al., 2003). Furthermore, iron (III) atoms in the substrate acted as nucleation sites for PPy formation (Vaeth and Jensen, 2000). Thin and uniform PPy layers were formed under vacuum because of faster VDP kinetics. Lower pressure in the VDP chamber allowed for faster monomer diffusion and a higher polymerization rate, which ultimately affected the morphology of the PPy film (Kwon et al., 2012c).

Fig. S2 illustrates the process of attaching antibodies to N-doped PPy carbon nanofibers (PPyNFs) and the resulting morphological changes are shown in the SEM micrographs in Fig. 2. The N-fibers were generated by a two-step thermal process. The first step stabilizes the needle-like features of PPy so they maintain their shape through acid treatment and antibody attachment. Specifically, the PPyNFs were heated at 135 °C for 2 h in air. This process creates micro-crosslinks between PVA nanofibers and results in a higher degree of crystallinity and enhanced water resistance (Wong et al., 2010; Wijanarko et al., 2016). The second step consists of carbonization at 600 °C for 1 h in an atmosphere of flowing argon. These two processes result in thinner PPyNFs with a similar overall morphology, but with a rougher surface (Fig. 2a and d).

The carbonized PPyNFs (PCNFs) were then soaked in an acid solution to introduce oxygen-bearing functional groups, to allow for the attachment of anti-cortisol antibodies. The surface of acid-treated PCNFs (PCANFs) was functionalized by immersing the films in a 3:1 (v/v) mixture of 1 M sulfuric acid and 1 M nitric acid at room temperature for 6 h. (Fig. 2b and e). The 6-h immersion time was deemed optimal for maintenance of the surface morphology. Immersion in acid for longer than 21 h resulted in undefined and partially destroyed surface morphologies (Fig. S3). To attach antibodies, the PCANFs were then immersed in a mixture of dilute anti-cortisol antibodies in phosphate-buffered saline (PBS) and 1 wt% aqueous dimethethoxy-1,3,5-triazin-2-yl-4-methylmorpholimium chloride (DMT-MM) catalyst for 12 h, washed with distilled water, and dried at room temperature. The SEM micrograph in Fig. 2c shows antibody-labeled PCANFs created by vacuum VDP (VA_PCANFs). Similarly, Fig. 2f shows antibody-labeled PCANFs created using atmospheric-pressure VDP (AA_PCANFs). Both micrographs clearly show anti-cortisol antibodies as cotton ball-like shapes on the PCANF surface.

3.2. Characterization of N-doped carbon nanofiber transducers

Fourier-transform infrared (FT-IR) spectroscopy was used to confirm changes in chemical functionality associated with the various chemical treatments (Fig. 3a). The major characteristic peaks of PVA and PPy are clearly observed in the FT-IR spectrum of PPyNF. The peaks associated with PPy at 1549, 1424, 1046, 968 and 794 cm^{-1} correspond to C=C, C-C, and C-N stretches, and C-H in-plane and C-H out-of-plane vibrations, respectively. PVA-based features include a peak at 3219 cm^{-1} (-OH stretching of the hydroxyl group), 2925 cm^{-1} ($-CH_2$ asymmetric stretch), 1697 cm^{-1} (C=O carbonyl stretch), 1621 cm^{-1} (C-H bending vibration), 1375 cm^{-1} (C-H deformation vibration), 1070 cm^{-1} (C-O stretching of the acetyl group), and 840 cm^{-1} (C-C stretching). The FT-IR spectrum of PCNFs showed less intense peaks associated with PVA and PPy, except for the –OH hydroxyl peak at 3450 cm^{-1}. The persistent prominence of this peak indicates that the oxygen atoms in PVA reacted with surrounding atoms during carbonization, and that a small amount of PVA remained after carbonization. Conversely, the FT-IR spectrum of PCANF contained several peaks corresponding to the presence of various oxygen-bearing functional groups at 3450 (-OH stretching of the hydroxyl group), 1743 (C=O stretch) and 1169 (C-O stretch) cm^{-1}.

The Raman spectra of carbon materials feature two principal peaks, the D peak and the G peak, that allow relative analysis of structural organization, as shown in Fig. 3b. The D peak at 1340 cm^{-1} corresponds to disordered sp^2 carbon, while the G peak at 1580 cm^{-1} corresponds to well-ordered, or graphitic, phases. The spectrum of PPyNF also contained two characteristic peaks at 1374 cm^{-1} and 1602 cm^{-1}, which were assigned to the C-N stretching and C=C backbone

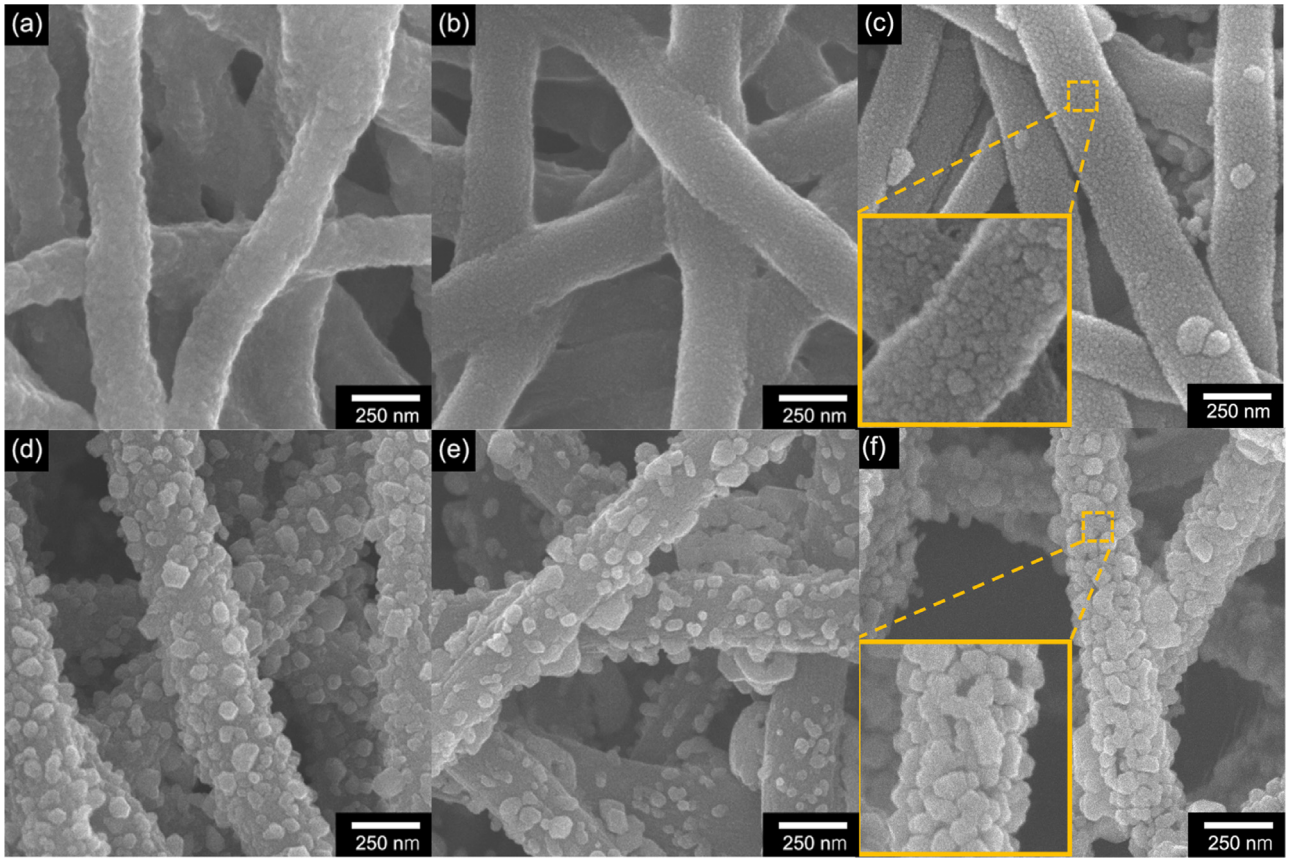

Fig. 2. The SEM images of (a) PCNFs, (b) PCANFs, and (c) antibody attached PCANFs from vacuum VDP step (VA_PCANFs). And the SEM images of d) PCNFs, e) PCANFs, and f) antibody attached PCANFs from atmospheric VDP step (AA_PCANFs).

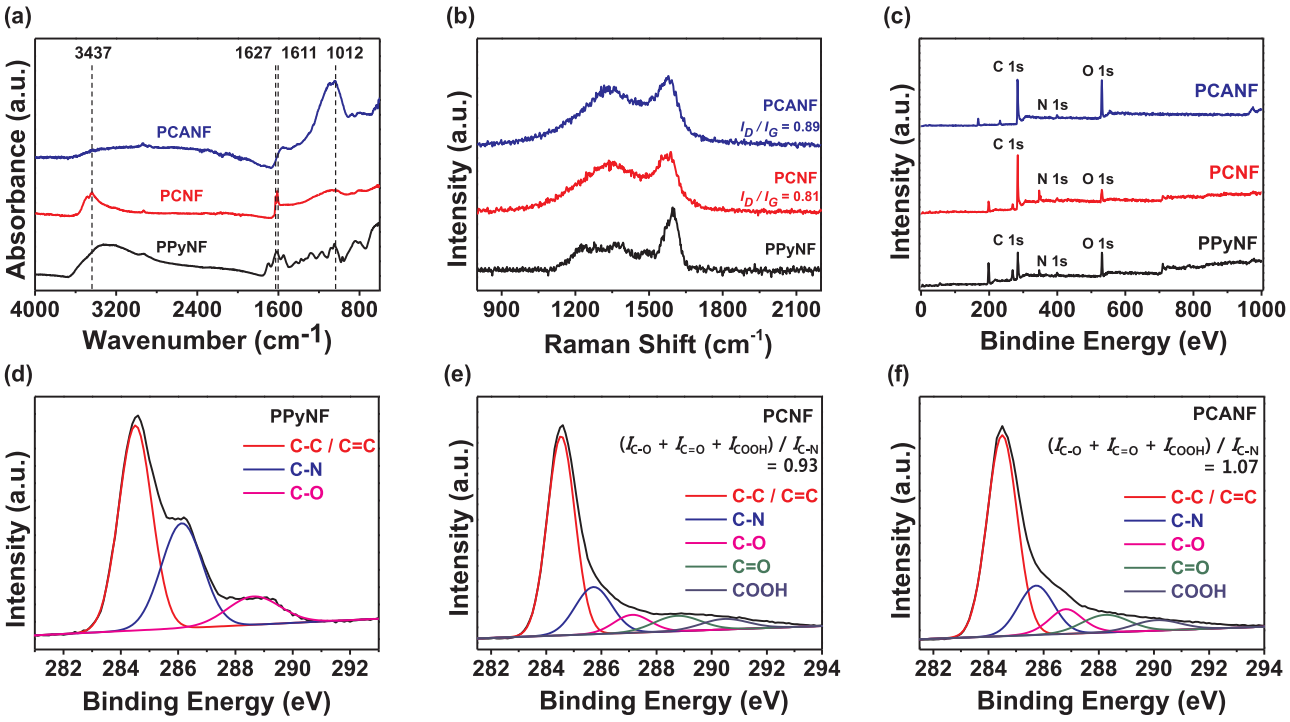

Fig. 3. (a) Fourier transform infrared (FT-IR) spectra (b) Raman spectra c) X-ray photoelectron spectroscopy (XPS) spectra of PPyNF (black), PCNF (red) and PCANF (blue). High-resolution C 1s spectra of (d) PPyNF, (e) PCNF and (f) PCANF.

stretching vibrations of pyrrole rings, respectively (Na et al., 2016). The intensity ratio (I_D/I_G) can be used as an index of the degree of crystallinity in carbon materials (Jyongsik and Joonwon, 2004). The I_D/I_G ratio of PCNF was 0.81. This is similar to values of approximately 0.80 that have been measured with other carbonized carbon materials (Jyongsik and Joonwon, 2004; Jang and Oh, 2004). After acid treatment, the I_D/I_G ratio of PCANF increased to 0.89, which indicates the introduction of structural defects into the carbon backbone. The D and G peaks were also shifted slightly following thermal and acid treatments, due to structural changes and π-π interactions between the PPy backbone and oxygen-bearing functional groups.

The chemical compositions of PPyNF, PCNF and PCANF were investigated by X-ray photoelectron spectroscopy (XPS). The overall XPS spectra contained peaks at around 285.1, 400.7 and 532.0 eV, corresponding to the C (1s), N (1s) and O (1s) orbitals of PPy and oxygen-bearing functional groups, respectively, as shown in Fig. 3c. The PPyNF and PCNF spectra contained residual peaks associated with $FeCl_3$ in the oxidative solution. Peaks at 710, 269 and 198 eV correspond to Fe (2p), Cl (2s) and Cl (2p) orbitals, respectively. The peak at 233 eV denotes the S (2s) orbital, while that at 169 eV denotes the S (2p) orbital. Both of these peaks derive from the sulfuric acid solution used to generate PCANF. The high-resolution XPS spectrum of the C (1s) orbital around 284.1 eV was deconvolved to differentiate chemical environments of carbon in the various PPyNF films (Fig. 3d–f). The three peaks at 284.5, 286.1 and 288.6 eV indicate the presence of C-C/C=C, C-N and C-O bonds, respectively, in pyrrole and in the PVA electrospun fibers (Fig. 3d). The C (1s) peaks of PCNF and PCANF were deconvolved into five peaks assigned to C-C/C=C (284.5 eV), C-N (285.7 eV), C-O (286.8 eV), C=O (288.2 eV), and COOH (290.1 eV) bonds (Fig. 3e and f). The XPS spectrum of PCNF contained several peaks corresponding to oxygen-bearing functional groups. In agreement with the FT-IR spectra, these data indicate that PVA reacted with surrounding atoms during carbonization. The intensity ratio ($I_{C\text{-}O} + I_{C=O} + I_{COOH}/I_{C\text{-}N}$) of PCNF was calculated as 0.93. This increased to 1.07 following acid treatment to generate PCANF. These data indicate an increase in the number of oxygen-bearing functional groups following acid treatment.

3.3. Characterization of PCANF FET-based biosensors

Fig. 4a and Fig. S4 shows a schematic diagram of the liquid-ion gated FET-based biosensor system. The biosensor was constructed with an interdigitated array (IDA) substrate array using antibody-labeled PCANFs (VA_PCANFs and AA_PCANFs) as signal transducers. The transducers were immobilized by covalent bonds with the IDA surface from a liquid electrolyte consisting of PBS (pH 7.4) solution. The gate electrode (V_g) was submerged in the electrolyte to allow control of the gate potential. Two gold bands were used as the source (s) and drain (d) electrodes. The device fabrication procedure is explained in detail in the Experimental Section.

The electrical performance of VA_PCANFs and AA_PCANFs on gold electrode substrates was characterized by obtaining current-voltage (I_{sd} –V_{sd}) curves over a range of –0.5 V to + 0.5 V at a gate voltage (V_G) of 0 V, as shown in Fig. 4b. The linearity of the I_{sd} –V_{sd} curves indicates Ohmic contact between the antibody-labeled transducers and the gold electrode, indicative of strong covalent bonding (Na et al., 2016; Jun et al., 2014). In general, the carbon nanofibers exhibited excellent electrical properties. However, dI/dV decreased slightly with every chemical treatment. This is because increasing the amount of oxygen-bearing functional groups and further antibody labeling decreased the overall conductivity of the fibers. Nevertheless, the linearity of the I_{sd}–V_{sd} curves was maintained even after functionalization and antibody labeling, which indicates minimal perturbation of electrical contacts and conductivity. Furthermore, the electrical properties of VA_PCANF exhibited a similar trend to that of AA_PCANF, as shown in Fig. S5a.

The source-drain current (I_{sd}) and source-drain voltage (V_{sd}) of PCNAF devices were measured under various V_G between −0.4 V and +1.0 V in increments of 0.2 V. The resulting data, shown in Fig. 4c and Fig. S5b, demonstrate the charge transport properties of VA_PCANFs and AA_PCANFs in our FET-based biosensor system. I_{sd} became more positive with increasing V_G, as is typical for n-type transistors. Although PPy materials typically exhibit p-type semiconductor behavior, our PCANF transducers showed stable n-type (electron-transporting) behavior after nitrogen-doping (Kwon et al., 2012a). This is because nitrogen doping into the carbon lattice during carbonization yields semimetallic properties, including a vanishing or narrow band gap (Krstić et al., 2007; Xiao et al., 2005). In addition, electron-rich nitrogen species can produce n-type transistor behaviors in a carbon matrix (Wang et al., 2009). These results indicate that our VA_PCANFs and AA_PCANFs FET sensors are suitable as electrochemical biosensors for detecting charged biomolecules in a PBS buffer solution.

3.4. Real-time response of A-PCANFs FET-based biosensors

The real-time performance of our PCANF FET-based biosensors was assessed by measuring changes in current as a function of cortisol concentration at constant V_{sd} (0.7 V) and V_G (0.005 V). Fig. 5a shows data collected for both VA_PCANF and AA_PCANF transducers. Each biosensor device responded immediately (< 1s) to changes in cortisol concentration. Mulchandani et al. suggested that the number of hole carriers decreases upon binding of cortisol to antibodies on p-type single-walled carbon nanotubes (Tlili et al., 2011). Furthermore, it is possible that nitrogen atoms doped into carbon nanofibers act as electron donors upon antigen-antibody binding (Gruner, 2006). Specifically, the binding event following analyte injection induces a positive charge near the transducer surface at the interface with the liquid-ion gate dielectric. The accumulation of negative electron carriers

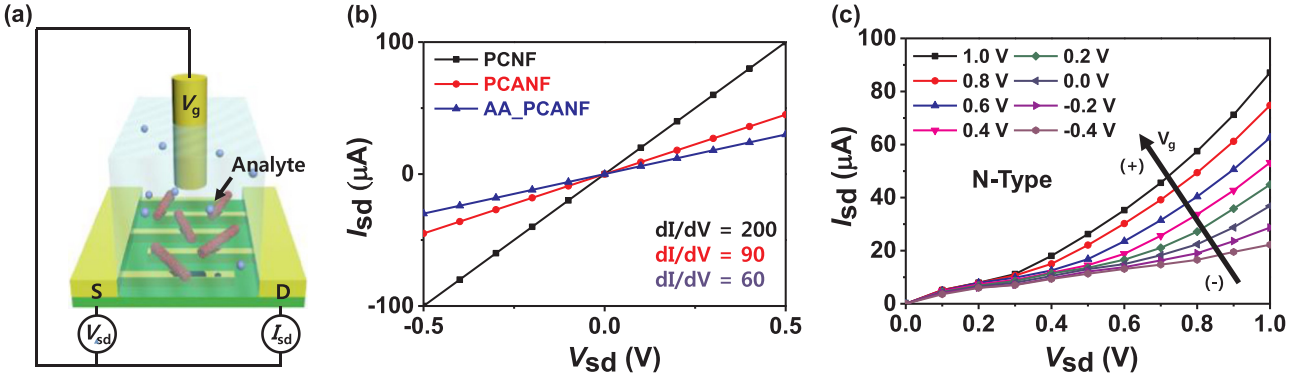

Fig. 4. (a) Schematic diagram of liquid-ion-gated FET sensor with A_PCANFs. (b) Source-drain current-voltage (I_{sd}–V_{sd}) curves of PCNF, PCANF and AA_PCANF. (c) Source-drain current-voltage (I_{sd}–V_{sd}) curves of AA_PCANF FET sensor electrode according to various gate voltage (V_G) ranging from -0.4 V to 1.0 V in every 0.2 V step.

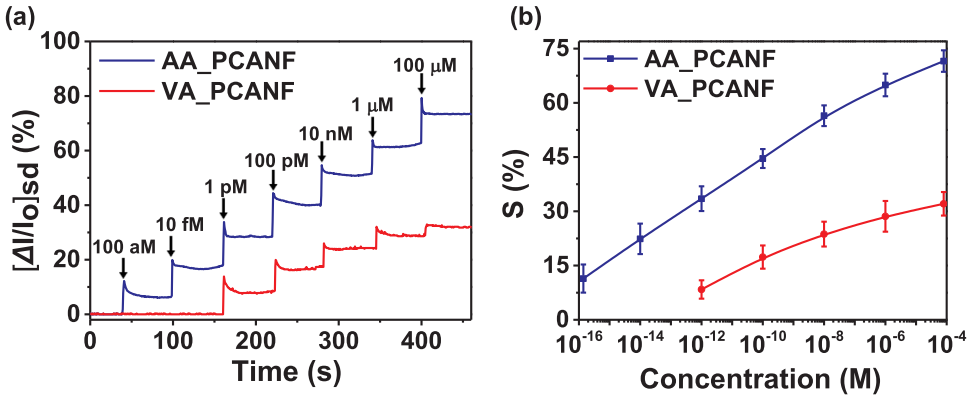

Fig. 5. (a) Real-time responses and (b) calibration curve of the AA_PCANF and VA_PCANF FET sensors as various concentrations of cortisol solution.

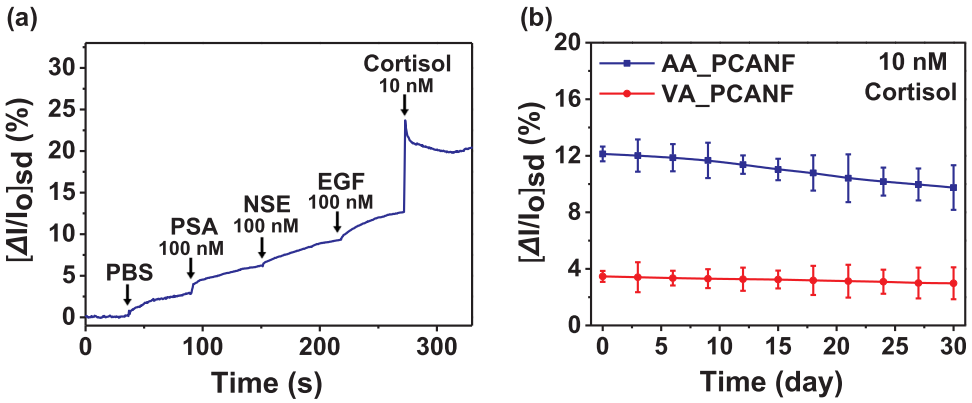

Fig. 6. (a) Real-time response for the selectivity test of non-target (PBS, PSA, NSE, EGF) and target (cortisol) materials and (b) stability and reusability test of AA_PCANFs and VA_PCANFs biosensor at 10 nM of cortisol concentration over 1 month.

consequently induces a current increase in n-type conductive channels.

The response of our AA_PCANF-based biosensors was greater than that of our VA_PCANF-based biosensors and was extremely sensitive to cortisol with a minimum detection limit of 100 aM at room temperature. Compared to the smooth surface of VA_PCANF, the needle-like structures of the AA_PCANF film resulted in a much higher available surface area for antibody binding. The minimum detection limit for cortisol on AA_PCANF-based biosensors was 10^4 times lower than that of VA_PCANF-based sensors (1 pM). Fig. 5b shows changes in sensitivity as a function of cortisol concentration. Sensitivity (S) was determined by the saturation point of the normalized current change during calibration, measured about 30 s after analyte addition. The AA_PCANF-based biosensors exhibited a linear detection range from 100 aM to 10 nM with a regression coefficient of 0.998, while the response of VA_PCANF did not show clear linear line, namely the response of AA_PCANF to cortisol was linear over a much broader range of cortisol concentrations than was the response of VA_PCANF. Moreover, Table S1 presents the analytical performance of various cortisol electrochemical biosensors in detail. The AA_PCANF-based biosensors hereby demonstrated impressive performance as better sensitivity, lower detection limit and wider linear range.

The selectivity of our AA_PCANF-based FET biosensors to cortisol was investigated by real-time monitoring of I_{sd} in the presence of several related proteins and other potential biological interferents, including PBS, prostatic-specific antigen (PSA), neuron-specific enolase (NSE) and epidermal growth factor (EGF), as shown in Fig. 6a. A remarkable increase in current occurred after cortisol injection, even in the presence of vast excesses of interferent. Exposure to PSA, NSE or EGF solutions did not illicit a change in charge density on the transducer surface. These results show that the AA_PCANF FET-based biosensor is specific for cortisol.

The reusability and stability of our VA_PCANF and AA_PCANF FET-based biosensors were assessed by monitoring changes in transducer current as a function of time at constant cortisol concentration (10 nM), as shown in Fig. 6b. Injections of cortisol were performed several times at 3-day intervals. The response of the cortisol biosensors decreased slightly over the course of 1 month, indicating good reproducibility. Specifically, sensor sensitivity decreased by ca. 19.6% for AA_PCANFs and ca. 14.0% for VA_PCANFs because of partial antibody inactivation or collapse of the transducer. Nevertheless, the covalent interaction between the PCANF film and the antibody was functionally stable at room temperature.

Fig. S6 shows data collected in a real-world application of our PCANF-based biosensors. These data indicate that our AA_PCANF FET-based biosensors are appropriate for real-time measurement of cortisol levels in saliva.

4. Conclusions

The high-performance biosensor was developed for cortisol detection using N-doped carbon nanofibers-based FET. We preferentially introduced multidimensional morphology to carbon nanofibers by the extremely facile methods, vapor deposition polymerization (VDP), to effectively enhance the surface area. Changing the just one deposition parameters during VDP considerable affected the surface morphology of the conducting polymer. As the signal transducer in a liquid ion-gate FET based cortisol biosensor, the N-doped multidimensional carbon nanofibers were functionalized by thermal, acid treatments and antibody attachment with without any damage of their morphology. Then, we demonstrated how much the difference of surface area influenced on the performance of electrochemical biosensor. The fabricated biosensor exhibited a low detection limit of 100 aM and a linear detection range

from 100 aM to 10 nM with a regression coefficient of 0.998. The results in this study can be extended for detection of salivary cortisol without any pretreatment at the point-of-care application.

CRediT authorship contribution statement

Goeen Jeong: Data curation, Formal analysis, Investigation, Validation, Visualization, Writing - original draft, Writing - review & editing. **Jungkyun Oh:** Conceptualization, Formal analysis, Methodology, Project administration, Writing - review & editing.

Acknowledgements

This research was supported by Device Business, Samsung Electronics, Korea.

Declaration of interest

The authors declare that they have no known competing financial interests or personal relationships that could have appeared to influence the work reported in this paper.

Appendix A. Supplementary material

Supplementary data associated with this article can be found in the online version at doi.org/10.1016/j.bios.2019.01.061.

References

Ahn, S.R., An, J.H., Song, H.S., Park, J.W., Lee, S.H., Kim, J.H., Jang, J., Park, T.H., 2016. ACS Nano 10 (8), 7287–7296.
An, J.H., Jang, J., 2017. Nanoscale 9 (22), 7483–7492.
Arya, S.K., Chornokur, G., Venugopal, M., Bhansali, S., 2010a. Procedia Eng. 5, 804–807.
Arya, S.K., Chornokur, G., Venugopal, M., Bhansali, S., 2010b. Biosens. Bioelectron. 25 (10), 2296–2301.
Bai, X., Hu, X., Zhou, S., Yan, J., Sun, C., Chen, P., Li, L., 2011. J. Mater. Chem. 21 (20), 7123–7129.
Brownlie, L., Shapter, J., 2018. Carbon 126, 257–270.
Cho, J., Shin, K.-H., Jang, J., 2010. Thin Solid Films 518 (18), 5066–5070.
Cook, N.J., Schaefer, A.L., Lepage, P., Morgan Jones, S.D., 1997. J. Agric. Food Chem. 45 (2), 395–399.
Corbalán-Tutau, D., Madrid, J.A., Nicolás, F., Garaulet, M., 2014. Physiol. Behav. 123, 231–235.
Di Valentin, C., Finazzi, E., Pacchioni, G., Selloni, A., Livraghi, S., Paganini, M.C., Giamello, E., 2007. Chem. Phys. 339 (1), 44–56.
Gangopadhyay, R., Chowdhury, A.D., De, A., 2012. Sens. Actuator B-Chem. 171–172, 777–785.
Geier, M.L., Moudgil, K., Barlow, S., Marder, S.R., Hersam, M.C., 2016. Nano Lett. 16 (7), 4329–4334.
Gokoglan, T.C., Soylemez, S., Kesik, M., Dogru, I.B., Turel, O., Yuksel, R., Unalan, H.E., Toppare, L., 2017. Food Chem. 220, 299–305.
Gruner, G., 2006. Anal. Bioanal. Chem. 384 (2), 322–335.
Gupta, S., Murthy, C.N., Prabha, C.R., 2018. Int. J. Biol. Macromol. 108, 687–703.
Jang, H.-J., Lee, T., Song, J., Russell, L., Li, H., Dailey, J., Searson, P.C., Katz, H.E., 2018. ACS Appl. Mater. Interfaces 10 (19), 16233–16237.
Jang, J., Oh, J.H., 2004. Chem. Commun. 7, 882–883.
Jang, J., Lim, B., Choi, M., 2005. Chem. Commun. 33, 4214–4216.
Jun, J., Lee, J.S., Shin, D.H., Jang, J., 2014. ACS Appl. Mater. Interfaces 6 (16), 13859–13865.
Jyongsik, J., Byungkwon, L., 2003. Angew. Chem. Int. Ed. 42 (45), 5600–5603.
Jyongsik, J., Joonwon, B., 2004. Angew. Chem. Int. Ed. 43 (29), 3803–3806.
Kaushik, A., Vasudev, A., Arya, S.K., Bhansali, S., 2013. Biosens. Bioelectron. 50, 35–41.
Kim, J., Sohn, D., Sung, Y., Kim, E.-R., 2003. Synth. Met. 132 (3), 309–313.
Kim, K.S., Jang, J.-R., Choe, W.-S., Yoo, P.J., 2015. Biosens. Bioelectron. 71, 214–221.
Kim, Y.-H., Lee, K., Jung, H., Kang, H.K., Jo, J., Park, I.-K., Lee, H.H., 2017. Biosens. Bioelectron. 98, 473–477.
Krstić, V., Rikken, G.L.J.A., Bernier, P., Roth, S., Glerup, M., 2007. EPL (Europhys. Lett.) 77 (3), 37001.
Kwon, O.S., Park, S.J., Jang, J., 2010. Biomaterials 31 (17), 4740–4747.
Kwon, O.S., Park, S.J., Hong, J.-Y., Han, A.R., Lee, J.S., Lee, J.S., Oh, J.H., Jang, J., 2012a. ACS Nano 6 (2), 1486–1493.
Kwon, O.S., Park, S.J., Lee, J.S., Park, E., Kim, T., Park, H.-W., You, S.A., Yoon, H., Jang, J., 2012b. Nano Lett. 12 (6), 2797–2802.
Kwon, O.S., Park, S.J., Park, H.-W., Kim, T., Kang, M., Jang, J., Yoon, H., 2012c. Chem. Mater. 24 (21), 4088–4092.
Lee, J.E., Lee, Y., Ahn, K.-J., Huh, J., Shim, H.W., Sampath, G., Im, W.B., Huh, Y.I., Yoon, H., 2015. Sci. Rep. 5, 8420.
Li, G., Jiang, L., Peng, H., 2007. Macromolecules 40 (22), 7890–7894.
Machida, S., Miyata, S., Techagumpuch, A., 1989. Synth. Met. 31 (3), 311–318.
Manickam, P., Pasha, S., Snipes, S., Bhansali, S., 2017. J. Electrochem. Soc. 164 (2), B54–B59.
Moraes, A., Kubota, L., 2016. Chemosensors 4 (4), 20.
Na, W., Park, J.W., An, J.H., Jang, J., 2016. J. Mater. Chem. B 4 (29), 5025–5034.
Powell, D., Chandra, S., Dodson, K., Shaheen, F., Wiltz, K., Ireland, S., Syed, M., Dash, S., Wiese, T., Mandal, T., Kundu, A., 2017. Eur. J. Pharm. Biopharm. 114 (Supplement C), 108–118.
Punetha, V.D., Rana, S., Yoo, H.J., Chaurasia, A., McLeskey, J.T., Ramasamy, M.S., Sahoo, N.G., Cho, J.W., 2017. Prog. Polym. Sci. 67, 1–47.
Sarkar, M., Das, B.C., Bora, B.D., Kumar, V., Mohan, K., Meyer, H.H.D., Prakash, B.S., 2007. Gen. Comp. Endocrinol. 154 (1–3), 85–90.
Shin, D.H., Lee, J.S., Jun, J., Jang, J., 2014. J. Mater. Chem. A 2 (10), 3364–3371.
Son, M., Kim, D., Park, K.S., Hong, S., Park, T.H., 2016a. Biosens. Bioelectron. 78, 87–91.
Son, M., Kim, D., Park, K.S., Hong, S., Park, T.H., 2016b. Detection of aquaporin-4 antibody using aquaporin-4 extracellular loop-based carbon nanotube biosensor for the diagnosis of neuromyelitis optica. Biosens. Bioelectron. 78, 87–91.
Sun, B., Gou, Y., Ma, Y., Zheng, X., Bai, R., Ahmed Abdelmoaty, A.A., Hu, F., 2017. Biosens. Bioelectrons. 88 (15), 55–62.
Supaphol, P., Chuangchote, S., 2008. J. Appl. Polym. Sci. 108 (2), 969–978.
Thapa, A., Soares, A.C., Soares, J.C., Awan, I.T., Volpati, D., Melendez, M.E., Fregnani, J.H.T.G., Carvalho, A.L., Oliveira, O.N., 2017. ACS Appl. Mater. Interfaces 9 (31), 25878–25886.
Tlili, C., Myung, N.V., Shetty, V., Mulchandani, A., 2011. Biosens. Bioelectron. 26 (11), 4382–4386.
Vaeth, K.M., Jensen, K.F., 2000. Chem. Mater. 12 (5), 1305–1313.
Wang, X., Li, X., Zhang, L., Yoon, Y., Weber, P.K., Wang, H., Guo, J., Dai, H., 2009. Science 324 (5928), 768–771.
Wijanarko, T.A.W., Kusumaatmaja, A., Chotimah, Roto, Triyana, K.,, 2016. AIP Conf. Proc. 1755 (1), 150010.
Wong, K.K.H., Zinke-Allmang, M., Wan, W., 2010. J. Mater. Sci. 45 (9), 2456–2465.
Xiao, K., Liu, Y., Hu, Pa, Yu, G., Sun, Y., Zhu, D., 2005. J. Am. Chem. Soc. 127 (24), 8614–8617.
Zhao, Y., Zhang, Z., Ren, Y., Ran, W., Chen, X., Wu, J., Gao, F., 2015. J. Power Sources 286, 1–9.
Zhao, Y.P., Fortin, J.B., Bonvallet, G., Wang, G.C., Lu, T.M., 2000. Phys. Rev. Lett. 85 (15), 3229–3232.